Contents lists available at SciVerse ScienceDirect

Applied Catalysis B: Environmental

Low temperature synthesis and photocatalytic properties of highly oriented ZnO/TiO$_{2-x}$N$_y$ coupled photocatalysts

Yunfang Huang [a,b,*], Yuelin Wei [a], Jihuai Wu [a], Chongshen Guo [b], Ming Wang [b], Shu Yin [b], Tsugio Sato [b]

[a] Engineering Research Center of Environment-Friendly Functional Materials, Ministry of Education; Huaqiao University, Xiamen, 361021, China
[b] Institute of Multidisciplinary Research for Advanced Materials, Tohoku University, 2-1-1, Katahira, Aoba-ku, Sendai, Japan, and Toyota Central R&D Laboratories Inc., Nagakute, Aichi 480-1192, Japan

ARTICLE INFO

ABSTRACT

A novel photocatalysts, ZnO thin film with nanotube arrays was prepared via soft solution route without any polymer additives and subsequently using a facile chemical etching of ZnO nanorods arrays along the *c*-axis. The thin film of large-scale ZnO arrays could be produced directly on the glass substrates. Scanning electron microscopy, diffuse reflectance spectra and X-ray diffraction were systematically used to confirm the successful fabrication of the patterns and to characterize the structure and morphology. The possible mechanism to form the ZnO nanotube array via such a facile approach was also discussed. Moreover, nitrogen doped titania (TiO$_{2-x}$N$_y$) as sensitizers were coupled with the ZnO nanotube and nanotube arrays in order to give the visible-light responsiveness. The investigation of photocatalytic ability proved that the ZnO nanotube arrays/TiO$_{2-x}$N$_y$ composites showed excellent photocatalytic activities for the decomposition of NO$_x$ gas under both visible-light and UV light irradiation, being superior to that of ZnO nanorods, ZnO nanotube, TiO$_{2-x}$N$_y$, commercial TiO$_2$ (AEROXIDE® P25) powders and ZnO nanorod arrays/TiO$_{2-x}$N$_y$ composites.

© 2012 Elsevier B.V. All rights reserved.

1. Introduction

ZnO is an exceptionally important material which possesses many unique optical and electrical properties for applications in wide research fields such as photocatalyst, solar cell, sensor, pigments, UV shielding material and so on [1–3]. The principles of these applications are quite similar, based on light absorption, light-electron conversion and electron transportation processes. The performance of these devices depends critically on the crystal structure, morphology and dimension of ZnO nanostructures, which determine the optical and electrical and thermal transport properties. Up to now, well-defined ZnO nanostructures with unique morphologies, such as nanorings [4], nanocombs [5], nanosprings [6], nanopropellers [7], tetrapod [8] and tetraleg [9] structures, have been reported. Various architectures with nanometer- and micrometer sized dimensions have been found to play an important role in achieving fast charge transfer and efficient charge separation for the improvement of photocatalytic activity. However, for the nanostructured ZnO based on interconnected dispersed particles, it is difficult to further improve the photocurrent efficiency due to charge-carrier recombination losses at grain boundaries between the nanoparticles. To avoid the recombination losses, one feasible method is to synthesize nanostructures which have a higher order degree compared to the random nanoparticles. A desirable morphology of the photocatalysts should have the mesoporous channels in parallel to each other and vertically with respect to the substrate such as nanorod/nanotube arrays. On the other hand, most applications of ZnO catalysts have been concentrated on suspension of ZnO particles in a solution [10–12]. However, the use of ZnO catalytic powders suffers limitations related to the filtering of the particles. Usually this requires either long time sedimentation or centrifugation processes. Preparation of ZnO well-aligned ZnO nanostructure firmly on the substrate with high stability and convenient reuse, will make it possible to overcome the disadvantage of difficulty in separation and to extend the industrial applications in environmental treatment.

Up to now, several methods have been reported to synthesize ZnO nanorod/nanotube arrays [13–16], including metal–organic chemical vapor deposition, thermal evaporation and template-based growth etc. Although these techniques are suitable for obtaining high-quality crystalline ZnO nanostructures, they require sophisticated and expensive instrumental systems, solid-state thermal sublimation process, and/or toxic source materials and

therefore may not be environmentally viable. It is highly desired to develop a facile synthesis process of morphology controlled ZnO photocatalysis with low-cost precursors and without special equipments, harsh experimental requirements or poisonous reagents. Compared to the above-mentioned methods, solution-phase methods are very attractive and popular because they can be performed with good productivity without using any rigorous conditions or sophisticated instrumentation. And the hydrothermal method is simple and economic for large-scale preparation of ZnO nanostructures [17,18]. It is generally accepted that the formation of zinc oxide superstructures in liquid media is more difficult than that by solid-state thermal sublimation process, because the crystalline growth in solution is mainly related to the comparatively low diffusion rate of ions and precipitation rate in liquid media, resulting in difficulty in rapid epitaxial growth. Vayssieres et al. [19] reported synthesis of ZnO microtubes on a range of substrates immersed in an aqueous solution containing equimolar amounts of zinc nitrate and methenamine and maintained at 90 °C for 2 days. Beside ZnO, some other nanorods such as a-FeO [20], Cr_2O_3 [21] and SnO_2 [22] can also be precipitated as condensed films with high ordering on the substrate.

In this work, we presented a novel seed growth process for fabrication of highly oriented ZnO nanorod/nanotube arrays over a large area in aqueous solution at low temperature (<100 °C) on the glasses substrates. This method allows large-scale grow aligned ZnO nanotubes on arbitrary substrate, which promotes the application and integration of ZnO nanomaterials. As we know, not only titanium oxide but also zinc oxide might be used as photocatalyst. In our previous research, it was found that nitrogen doped anatase type titania $TiO_{2-x}N_x$ showed excellent photocatalytic activity under visible light irradiation, due to narrowing band-gap energy by doping with nitrogen [23,24]. In the present research, in order to synthesize high active photocatalyst, the nano-scale superstructure ZnO was combined with nitrogen doped titania nanoparticles. It is expected that the composite of visible-light-responsive $TiO_{2-x}N_y$ and large surface area ZnO film with nano-scale superstructure show excellent photocatalytic activity. Photocatalytic destruction of NO is of great significance from the viewpoint of practical applications because NO is one of the typical pollutants in the exhaust gases from automobiles. We employed the destruction of NO as a model reaction to characterize the photocatalytic activity of the samples.

2. Experimental

All chemicals (analytical grade purity, Kanto, Chemical Co., Japan) were used as starting materials without further purification. Commercial borosilicate glass slides (Matsunami Glass Industries), 0.2 mm in thickness and 22 mm in diameter, were used as substrates. The arrays of ZnO nanotubes were synthesized by a simple two-step process.

2.1. ZnO seed layers preparation

The ZnO seed was prepared using a modified sol–gel method. 0.01 M ZnO colloid was prepared as following: 1.4 mmol lithium hydroxide and 1 mmol zinc acetate dihydrate were dissolved in 50 ml ethanol respectively. The lithium hydroxide solution was dropwised into the zinc acetate solution under magnetic stirring. The as-prepared colloidal ZnO nanocrystals were spin-coated on the glass substrates at 3000 rpm for 30 s. After processing, the glass substrates were heated at 100 °C for 30 min to remove the solvent. Before coating, the glass substrates were cleaned with acetone in an ultrasonic bath.

2.2. ZnO nanorod/nanotube arrays preparation

And then, ZnO nanorodes were grown by suspending the seeded substrates upside-down in a sealed bottle containing of zinc nitrate hydrate (0.1 M) and hexamethylenetetramine (denoted as HMT) (0.1 M) aqueous solution at 95 °C. After 3 h of reaction, the glass substrates were removed from the solution. After growth, the wafer was thoroughly rinsed with de-ionized water and suspended once again into a 90 ml solution containing ammonia (0.5 wt%) and cetyltrimethyl ammonium bromide (denoted as CTAB) (0.5 wt%) at room temperature for 3.5 h (etching step). Finally, the substrate was rinsed with deionized water and ethanol to remove any residual salt or amino complex, respectively, and vacuum dried at 60 °C for 12 h.

2.3. $ZnO/TiO_{2-x}N_y$ composite preparation

Nitrogen-doped titania with anatase single phase was prepared by a solvothermal reaction. $TiCl_3$ (Kanto Chem. Co. Inc. Japan) was used as a starting material. HMT was used as a nitrogen source. A desired amount of HMT and 21.5 cm³ of 20 wt% $TiCl_3$ solution were mixed with 25 cm³ of pure methanol. The mixture was placed into a steel autoclave attached with a Teflon tube of internal volume of 200 cm³. The autoclave was heated and kept at 90 °C for 1 h to realize homogeneous precipitation and then heated at 190 °C for 2 h. The final pH value of the solution was adjusted to 9 by using HMT. The powder product was separated by centrifugation, washed with distilled water and acetone three times, then vacuum dried at 80 °C overnight. Then, the Nitrogen-doped titania coating was realized by spin coating at 3000 rpm for 15 s (Mikasa Spincoater 1H-D7). The coating liquid was prepared by uniformly mixing 1 g $TiO_{2-x}N_y$ powder with 2 g of nitrocellulose of industrial grade, 5 g of ethyl acetate and 5 g of butyl acetate using a paint shaker and 50 g of zirconia ball of 2.7 mm in diameter for 40 h. The binder in the film was removed by calcination at 400 °C for 1 h. Then, the growth of ZnO nanorod/nanotube arrays onto the surface of the TiO_2 film was prepared by repeating the step 1 and 2.

2.4. Photocatalytic reaction

According to the Japanese industrial standard (JIS standard) for photocatalytic $deNO_x$ reaction in 2004 [25], it is recommended that the activity of a photocatalyst should be characterized through measurement of the decrease in concentration of NO at the outlet of a flow reactor. In our work, photocatalytic activity during the oxidative destruction of nitrogen monoxide was determined by measuring the concentration of NO gas at the outlet of the reactor (373 cm³) during photoirradiation by a constant flow of 1 ppm NO-50 vol.% air (balanced N_2) mixed gas (200 cm³ min⁻¹) with a NO_x analyzer (Yanaco, ECL-88A). Two pieces of thin film photocatalyst sample of 22 mm in diameter, the total surface area of 760 mm², were set in the bottom center of the reactor. The inner cell was constructed from Pyrex glass, which served to filter out the UV emissions of the mercury arc with wavelengths less than 290 nm. A 450-W high-pressure mercury lamp was used as the light source, where the light wavelength was controlled by using filters such as Pyrex glass, Kenko L41 Super Pro (W) filter, and Fuji, triacetyl cellulose filter for cutting off the light of <290 nm, <400 nm, and <510 nm, respectively. The light wavelength distribution spectra of the high-pressure mercury light sources were measured using a multichannel spectrophotometer (JASCO, MD-100).

2.5. Characterization

The morphology and microstructure of the crystals were observed by a field-emission scanning electron microscope

(FE-SEM) (HITACHIS-4800). The size and shape of the nanoparticles were observed by transmission electron microscopy (TEM, JEOLJEM-2010). The crystalline phase of the products was determined by X-ray diffraction (XRD) analysis (SHIMADZU, XD-D1) using graphite-monochromized Cu Ka radiation. The diffuse reflectance spectra of the samples were measured using an UV–vis spectrophotometer (Shimadzu UV-2450). The nanotubes surface was observed by atomic force microscopy (AFM, Nanopics 1000 S II).

3. Result and discussion

3.1. Phase and morphology

Fig. 1 shows the field-emission scanning electron microscope (FE-SEM) images of the ZnO nanorod arrays grown on the substrate. The low-magnification image showed a large area uniform film-like material deposited on the substrate (Fig. 1(a)). Large-scale growth of nanomaterials is important in nanodevice fabrication. In the present work, we could overspread ZnO nanorods on the whole substrate. This result implies that our method is applicable to mass production of well-aligned ZnO nanorod arrays. From the high-magnification images (Fig. 1(b) and (c)), it could be seen that a high density of ZnO nanorods with well defined hexagonal facets (0 0 1) were grown vertically on the substrate. The nanorods had a narrow size distribution centered at about 200 nm in diameter. The cross-sectional view (Fig. 1(d)) of the nanorod arrays demonstrated that the ZnO nanorods grew vertically with identical length about 1.0 μm. The diameters and length of the nanorods could be tailored by controlling the growth parameters such as growth time, temperature, and zinc salt concentration. The diameter and length of nanorods were dependent on the growth parameters such as zinc salt concentration, growth temperature, pH, ZnO seed layer concentration and the spin-coating times.

Fig. 2 shows the FE-SEM images of ZnO nanotubes by selective etching of ZnO rods. The hexagonal ZnO nanotubes with a uniform wall thickness of about 20 nm and external diameter of 200 nm were observed. The ZnO nanotube arrays were predominantly aligned perpendicular to the substrate, and from the nanotubes aligned horizontal to the substrate the length of the nanotubes was calculated to be about 1.0 μm. Considering that the nanotubes were obtained from ZnO rods, their morphology would be considerably affected by the fabrication condition of ZnO rods. Since the nanotubes were evolved from the nanorods, the size of nanotubes were determined by the original ZnO nanorods, which could be readily controlled by tuning the reaction parameters such as Zn^{2+} ions concentration and growth time, etc. Therefore, it is possible to fabricate ZnO nanotubes with various sizes for different application by this method. The inset of Fig. 2(c) shows enlarged FE-SEM image of single nanotube, where completely tubular structure is found. Fig. 2(f) shows a typical TEM image of ZnO nanotubes. An obvious contrast between the tube wall and the inner part could be clearly observed, providing a direct evidence of the tubular structure, which was in agreement with the SEM observations. The selected area electron diffraction pattern of an individual ZnO nanotube (the inset in Fig. 2(f)) confirms that the ZnO nanotube is single crystalline.

The AFM measurements were performed by a commercial system (Nanopics 1000 S II). A typical topographic view of ZnO nanotubes array is shown in Fig. 3, which gives the size and the microstructure of the individual ZnO nanotubes. Scanning area is 20 μm × 20 μm. As shown in Fig. 3, the AFM image of a ZnO nanotube arrays exhibited larger diameters than those observed in SEM images. This distortion resulted from the tip convolution effect due to the high aspect ratio of the nanorods. We observed that the shapes of most particles are nearly columnar, and predominantly aligned perpendicular to the substrate.

Fig. 4(a) and (b) shows the corresponding XRD pattern of the ZnO nanorod and nanotube arrays grown on the glass substrate, respectively. The diffraction peaks could be well indexed to hexagonal
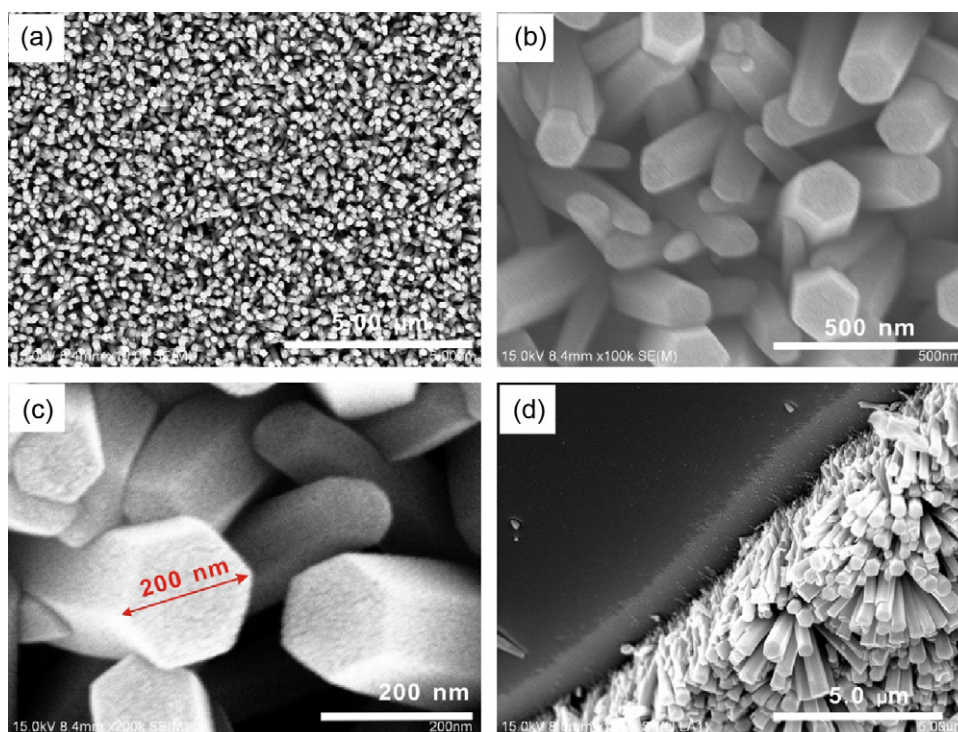

Fig. 1. FE-SEM images of the well-aligned ZnO nanorod arrays on the substrate. (a) Large-scale and low magnification, (b) and (c) fine structure of the nanorods under high magnification, (d) cross-sectional view.
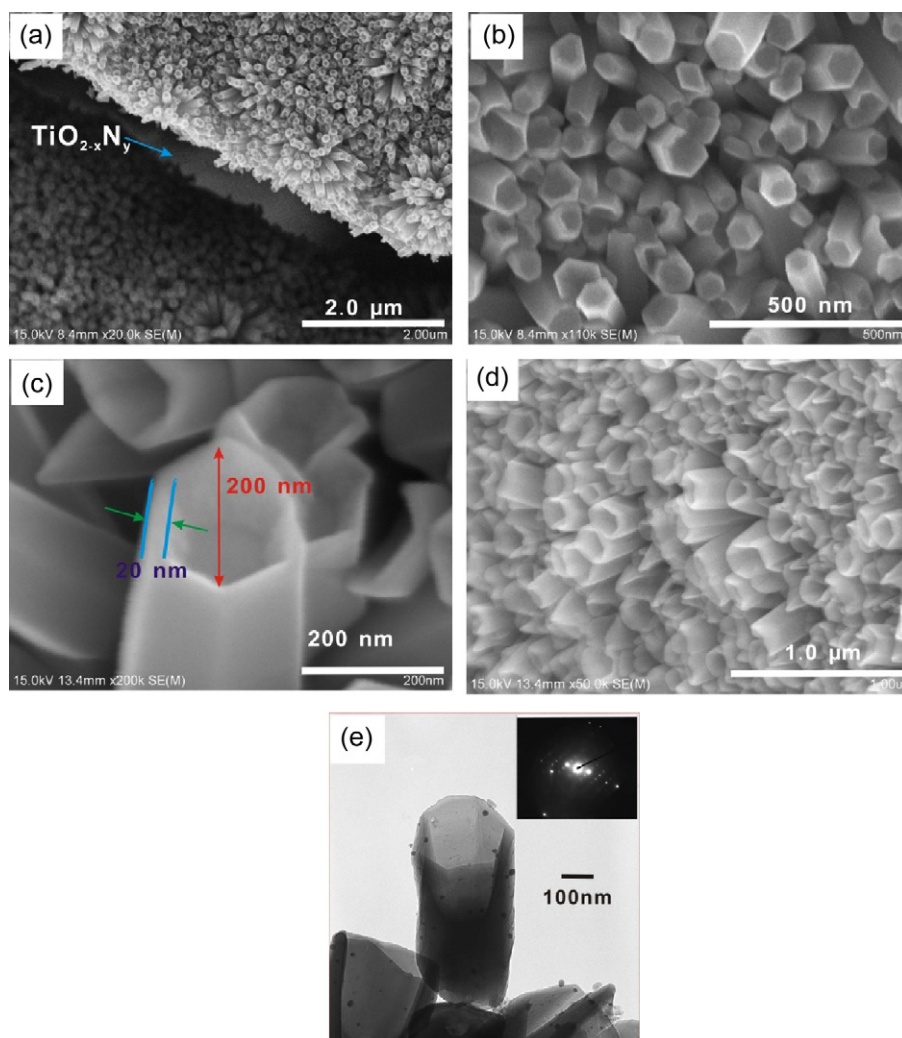
Fig. 2. FE-SEM images of the well-aligned ZnO nanotubes arrays on the substrate. (a) Large-scale and low magnification, (b) and (c) fine structure of the nanotubes under high magnification, (d) cross-sectional view, (e) TEM image of the ZnO nanotubes; the inset is the corresponding selected area diffraction pattern.
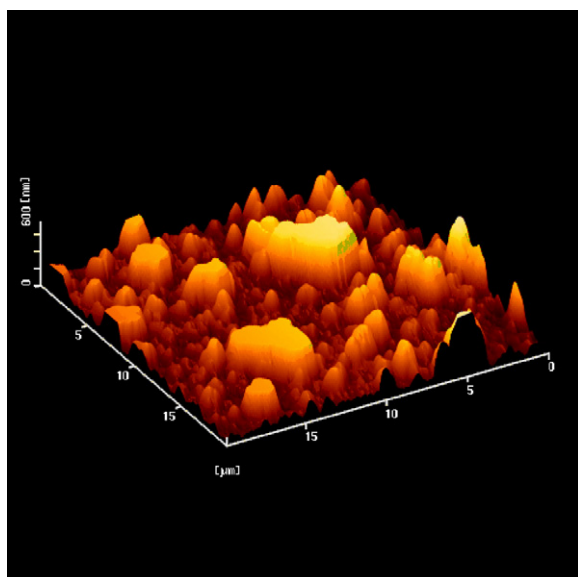

Fig. 3. Topographic view of AFM image of the well-aligned ZnO nanotubes arrays on the substrate. Scanning area is $20 \, \mu m \times 20 \, \mu m$.

wurtzite ZnO (JCPDS 65-3411), and no diffraction peaks from any other impurities had been detected in our samples. The intensity of the (0 0 2) peak was very strong compared with that of the other peaks such as (1 0 0) and (1 1 0). The result indicated the ZnO nanorod and nanotube arrays were highly aligned perpendicular to the substrate with c-axial growth direction. This result was consistent with that confirmed by SEM images, almost all the ZnO nanorods and nanotubes perpendicular to the surface of the substrate, which led to the strong diffraction of top surface such as (0 0 2).

As shown in Fig. 4(c), the XRD patterns of the $TiO_{2-x}N_y$ film sample indicated that the $TiO_{2-x}N_y$ film had a single phase of anatas with good crystallinity. It is interesting to note that the intensity of the (0 0 2) diffraction peak of ZnO for the $TiO_{2-x}N_y$/ZnO nanotube arrays composite film decreased substantially when compared with that for the pure ZnO nanotube arrays, and other peaks such as (1 0 0) and (1 1 0) were observed, indicated the ZnO nanorod and nanotube arrays were not highly aligned perpendicular to the substrate with c-axial growth direction. The slightly decreased oriented degree of the ZnO nanorod and nanotube arrays were mainly ascribed to the growth of the ZnO nanorods and nanotube arrays on the rough $TiO_{2-x}N_y$ film. As seen in Fig. 4(d), the titania peak from the $TiO_{2-x}N_y$/ZnO nanotube arrays composite film was also observed, indicating titania was actually mixed in the $TiO_{2-x}N_y$/ZnO nanotube arrays composite film.
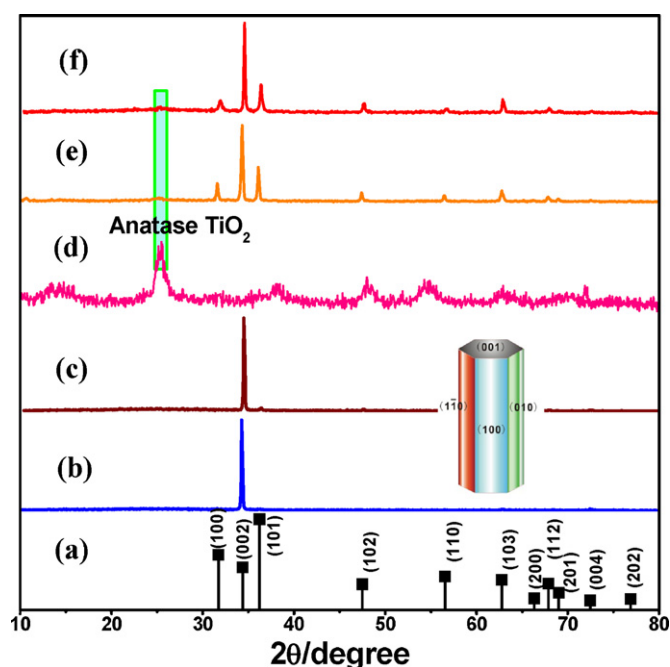
Fig. 4. XRD patterns of (a) standard ZnO (JCPDS No. 65-3411), (b) ZnO nanorod arrays on the glass substrate, (c) ZnO nanotube arrays on the glass substrate, (d) $TiO_{2-x}N_y$ film on the glass substrate (e) ZnO nanorod arrays/$TiO_{2-x}N_y$ composite on the glass substrate, (f) ZnO nanotube arrays/$TiO_{2-x}N_y$ composite on the glass substrate.

Fig. 5 shows the diffuse reflectance spectra of the prepared film. For a crystalline semiconductor, it was shown that the optical absorption near the band edge follows the equation [26,27]:

$$\alpha h\nu = A(h\nu - E_g)^{n/2} \qquad (1)$$

where a, ν, E_g, and A are absorption coefficient, light frequency, band gap, and a constant, respectively. The value of n decides the characteristics of the transition in a semiconductor. According to
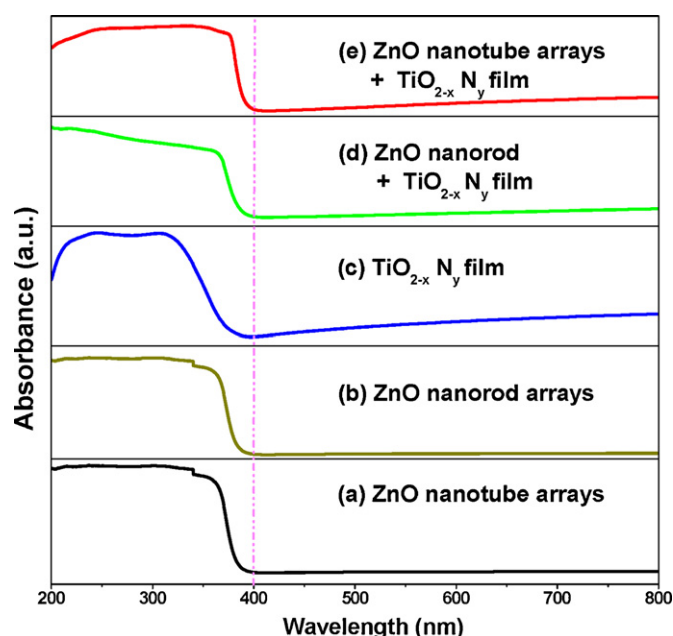

Fig. 5. DRUV–vis spectra of (a) ZnO nanotube arrays on the glass substrate, (b) ZnO nanorod arrays on the glass substrate, (c) $TiO_{2-x}N_y$ film on the glass substrate, (d) ZnO nanorod arrays/$TiO_{2-x}N_y$ composite on the glass substrate, and (e) ZnO nanotube arrays/$TiO_{2-x}N_y$ composite on the glass substrate.
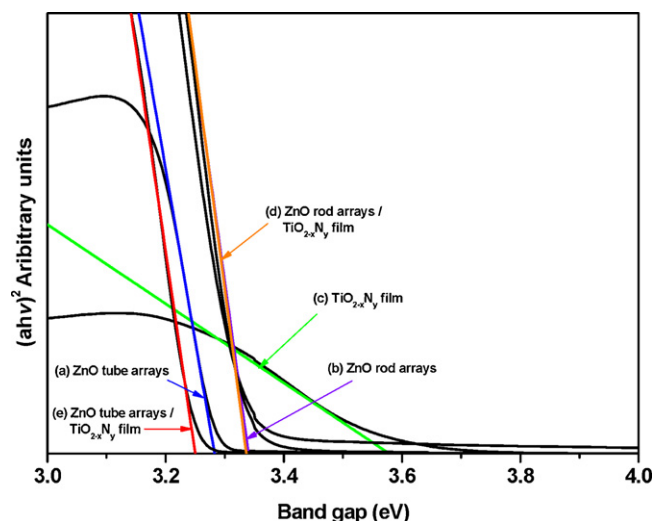

Fig. 6. Estimated band gap of (a) ZnO nanotube arrays on the glass substrate, (b) ZnO nanorod arrays on the glass substrate, (c) $TiO_{2-x}N_y$ film on the glass substrate, (d) ZnO nanorod arrays/$TiO_{2-x}N_y$ composite on the glass substrate, and (e) ZnO nanotube arrays/$TiO_{2-x}N_y$ composite on the glass substrate by Kubelka–Munk function. The band gaps of samples (a), (b), (c), (d) and (e) are determined as about 3.28, 3.96, 3.58, 3.33 and 3.25 eV at $(\alpha h\nu)^2 = 0$, respectively.

the equation the value of n for materials was 1. Fig. 6 shows the Mott–Schottky curves of samples. The direct optical band gaps of the films were determined by extrapolating the linear portion of each curve in Fig. 6 to $(\alpha h\nu)^2 = 0$. The band gaps of samples (a) ZnO nanotube arrays on the glass substrate, (b) ZnO nanorod arrays on the glass substrate, (c) $TiO_{2-x}N_y$ film on the glass substrate, (d) ZnO nanorod arrays/$TiO_{2-x}N_y$ composite on the glass substrate, and (d) ZnO nanotube arrays/$TiO_{2-x}N_y$ composite on the glass substrate are determined as about 3.28, 3.34, 3.58, 3.33 and 3.25 eV at $(\alpha h\nu)^2 = 0$, respectively. As shown in Fig. 5, in the UV light region, all samples presented a continuous wide absorption band. The steep shape of the visible edge and strong absorption in the visible region also indicated that the absorption band was attributable not to the transition from the impurity level to the conduction band, but to the intrinsic transition between the valence band and the conduction band, followed by long tailing due to scattering.

In our previous research, the synthesized $TiO_{2-x}N_y$ powder showed visible-light absorption in the range of 400–550 nm and possessed two absorption edges around 380–410 and 520–540 nm [24]. But in the present work, the $TiO_{2-x}N_y$ film on the glass substrate gave a band-gap of 3.58 eV. It may be due to the different material form and crystallization degree. The same results were also found by other research groups [28].

Compared with reported bulk-shaped ZnO (3.37 eV) [29], the decrease in the band gap energy of ZnO nanorod arrays (3.34 eV) and ZnO nanotube arrays (3.28 eV) was possibly due to the high crystallinity of the ZnO nanorod/nanotube arrays morphology on the surface of the substrate, and this conclusion was supported by data from other studies [30,31]. This could be attributed to the presence of an increased number of surface defects due to the anisotropic growth of the ZnO crystals. ZnO nanorods grown hydrothermally had inherent defects in the crystals in the form of vacancies and interstitials that allow visible light absorption.

The band gap of pure ZnO nanotube arrays was 3.28 eV, which was lower than that of pure ZnO nanorod arrays (3.34 eV). The red-shift of the light absorption of these ZnO nanotubes may be attributed to their special nanotube morphology. Similar observation had been reported on TiO_2 with nanotube morphology [32]. The degree of lattice distortion was likely to be relatively higher for nanotube arrays films, thus casing aggregation of vacancies acting
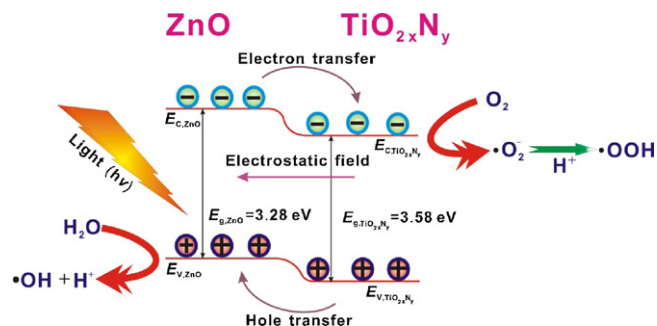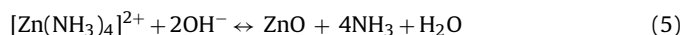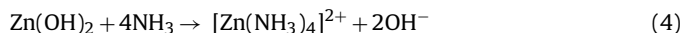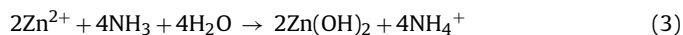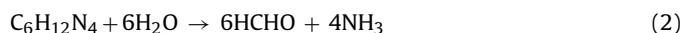
Fig. 7. Schematic illustration of the band structure and charge separation of the combined $ZnO/TiO_{2-x}N_y$ heterojunction.

as trap states along the seams of nanotube walls leading to a lower band-to-band transition energy.

Compared to that of pure ZnO nanorod and nanotube arrays, the red shift was observed on the band gap absorption edge of ZnO nanorod arrays/$TiO_{2-x}N_y$ composites and ZnO nanotube arrays/$TiO_{2-x}N_y$ composites, respectively. This was because (i) the $TiO_{2-x}N_y$ powders had visible-light absorption in the range of 400–550 nm due to the formation of N—Ti bonding in the $TiO_{2-x}N_y$ powders; (ii) the red shift of $ZnO/TiO_{2-x}N_y$ in longer-wavelength region was due to the contribution of heterojunction between ZnO and $TiO_{2-x}N_y$. As a result of the coupling of $TiO_{2-x}N_y$ with ZnO, it seemed that $TiO_{2-x}N_y$ may photosensitize ZnO in longer wavelength region. This permitted the novel photocatalyst to respond to a wide range of solar spectrum. What is notable, the light-responsive range was much wider than that of pure ZnO and $TiO_{2-x}N_y$ photocatalyst, and therefore they can more efficiently utilize lights for the photocatalytic purpose. The red shift of band gap absorption edge and the change of the E_g could be explained by the band gap theory. Fig. 7 shows the mechanism of the separation of electron–hole pairs. As illustrated in this scheme, although the band gap energies of ZnO and $TiO_{2-x}N_y$ are similar, the potentials of the conduction band and the valence band of ZnO charged a bit more negative. When ZnO combines with $TiO_{2-x}N_y$ to form complex semiconductor photocatalyst, upon band gap excitation, ZnO is excited first; the photogenerated electrons from ZnO are transferred into the conduction band of $TiO_{2-x}N_y$ at the heterojunction, which correspondingly changes the bottom of the conduction band, decreasing the band gap of the ZnO. On the other hand, the transfer of photogenerated hole also occurs from the valence band of $TiO_{2-x}N_y$ to that of ZnO, causing an oxidation reaction. Such an efficient charge separation increases the lifetime of the charge carriers and increases the efficiency of the interfacial charge transfer to adsorbed substrates.

Until now, although the growth mechanism of ZnO arrays is still not completely clear, we believe that the presence of well-aligned crystal nucleus on a substrate is the premise for growth of large-scale ZnO arrays. The growth mechanisms of ZnO crystals were discussed based on both the morphology evolution and the hydrolysis process in the precursor solutions. We can see that the formation of the nanotube arrays undergoes two steps, the growth and the surfactant-assisted etching of the ZnO nanorod arrays. In the growth step, tiny ZnO particles are deposited on the glass substrate in the very early stage on the gentle reaction condition. Then these ZnO particles would function as crystal nucleus for the subsequent growth of the ZnO arrays to form a large-scale ZnO rod arrays on the glass substrate. Here, we use HMT acting as a pH buffer to regulate the pH value of the solution and control the supply of OH^- accompanied with the increasing temperature. Through the whole experiment, the pH value keeps at about 6–7. HMT also as a homogeneous precipitation agent has been widely exploited

in synthesizing metal oxide nanostructures, of which the kinetics of nucleation, growth, and thus the morphology and structure of particles could be controlled by adjusting specimen concentration, reaction time, and temperature. It is accepted that the hydrolysis of HMT proceeds above 70 °C to produce ammonia and formaldehyde [33,34]. Ammonia reacts with zinc ions to produce $Zn(OH)_2$ and $Zn(NH_3)_4^{2+}$ (Eqs. (2)–(5)), which may be dehydrated and crystallized to form ZnO crystals [35,36]. The possible reactions discussed above can be described as follows:

$$C_6H_{12}N_4 + 6H_2O \rightarrow 6HCHO + 4NH_3 \tag{2}$$

$$2Zn^{2+} + 4NH_3 + 4H_2O \rightarrow 2Zn(OH)_2 + 4NH_4^+ \tag{3}$$

$$Zn(OH)_2 + 4NH_3 \rightarrow [Zn(NH_3)_4]^{2+} + 2OH^- \tag{4}$$

$$[Zn(NH_3)_4]^{2+} + 2OH^- \leftrightarrow ZnO + 4NH_3 + H_2O \tag{5}$$

The most stable crystal of ZnO is wurtzite structure consisting of polar $\{0\,0\,0\,1\}$ planes and non-polar $\{1\,0\,0\,0\}$ planes with C_{6v} symmetry. Due to the anisotropic crystal property, $[0\,0\,0\,1]$ of ZnO has the fastest growth velocity, and the growth rate under thermodynamic equilibrium hydrothermal conditions is $V[0\,0\,0\,1] > V[0\,1-1\,0] > V[0\,0\,0-1]$ [37,38]. With undercoat of ZnO seed particles on the substrate, the nanorods grow more readily and uniformly. Because of the polar nature of positively or negatively charged ZnO $\{0\,0\,0\,1\}$ planes, the surface will attract opposite charged ions on it and reacted to form ZnO nanorods.

In the growth stage, the equilibrium in Eq. (5) will shift to the right side because of the high concentration of $Zn(NH_3)_4^{2+}$. A large amount of the precursor $Zn(NH_3)_4^{2+}$ reacts with OH^- to form ZnO through hydrothermal decomposition, which is deposited on the substrate, leading to the formation of a single crystal ZnO nanorod. At the same time, ZnO also dissolves according to Eq. (4). So, in the etching step, when the ammonia is diluted with distilled water, the equilibrium will shift to the left side because of the high concentration of NH_3 at room temperature, resulting in ZnO nanotubes. On the other hand, the etching rates of the ZnO crystal along the c axis are faster than that in the other directions. NH_3 is a polar molecule, and there exists a lone pair of electrons in its electronic structure. Because ZnO surface is also negatively/positively charged, the polar molecules of NH_3 can be easily attached on. Generally, the positively Zn^{2+} terminated $(0\,0\,0\,1)$ and negatively O^{2-} terminated $(0\,0\,0-1)$ polar surfaces have high surface energies, and the growth/etching of the crystal is all preferentially along the c axis. Therefore, the electrostatic adhesion of NH_3 on ZnO nanorod is stronger, leading to a faster etching rate in polar surfaces. When the c-axis preferentially grown ZnO nanorods prepared in the growth step were soaked in aqueous NH_3 solution, the preferential adsorption of NH_3 molecules occurred on the $(0\,0\,0\,1)$ facets rather than on the lateral facets and OH^- were formed by the hydrolysis of NH_3. Subsequently, the OH^- anions reacted with ZnO to form a soluble hydroxyl complex such as $[Zn(OH)_4]^{2-}$ along the c axis. The selective dissolution of ZnO along the c-axis caused the formation of the tubes. However, for free etching (without the surfactant) after the etching away of the top area, etching along c axis becomes dominant. Therefore, the alternatively dominant etchings result in the shorter and shorter of the ZnO nanorod, and always with a shallow pit on the top end. It has been reported that CTAB can be used as effective agents to control the morphology of ZnO because CTAB is a cationic surfactant, resulting in the formation of a complex with the OH^- ion is easier than that with Zn^{2+} ions. Then, CTAB can be adsorbed on the lateral surface, prevent the further etching of the lateral surface of the ZnO nanorod, leading to the formation of the tubular structures, as schematically illustrated in Scheme 1.
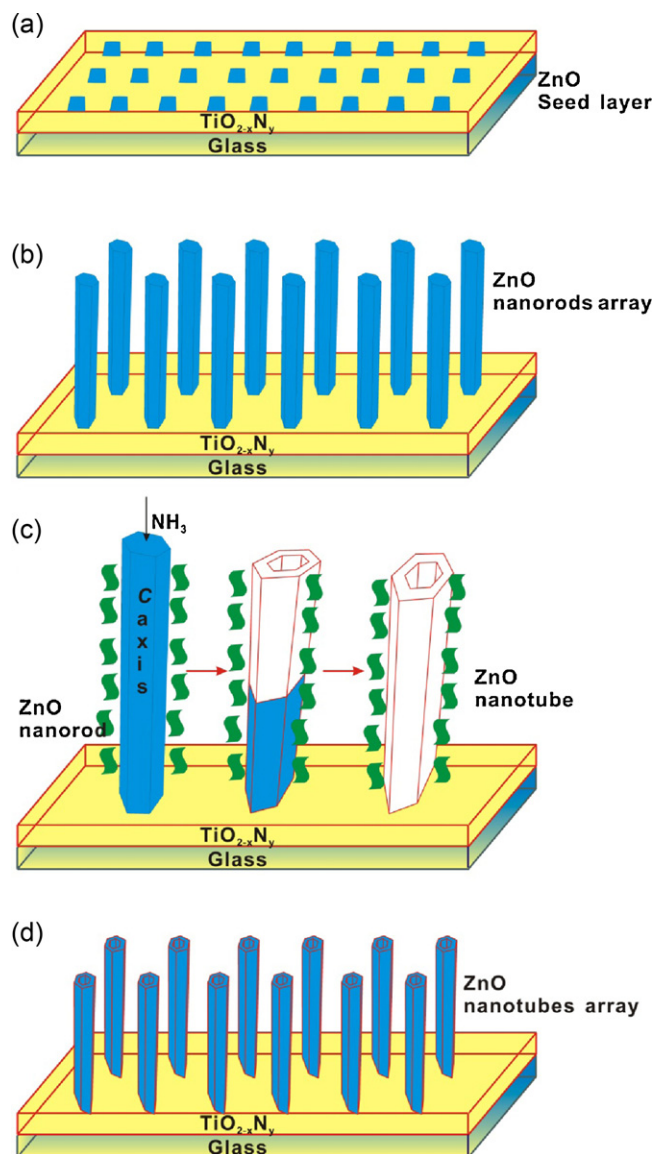
Scheme 1. Schematic showing the solution growth of highly oriented nanotubular array of ZnO onto the substrates: (a) sol–gel precursor spin-coating, (b) growth of vertically aligned ZnO nanorods via a hydrothermal method, (c) the chemical etching of ZnO nanorods array with the surfactant of CTAB, and (d) highly oriented nanotubular array of ZnO on the substrate after chemical etching.

3.2. Photocatalytic properties

To investigate the photocatalytic activity of the prepared samples, the oxidative photo-destruction of NO_x gas is performed. Fig. 8 shows the photocatalytic $deNO_x$ ability of the various samples, respectively. As a comparison, a standard commercial titania photocatalyst (Aeroxide® P25), which showed high photocatalytic activity, was also characterized. The light of the wavelength less than 290, 400 and 510 nm could be filtered out using a Pyrex glass jacket, 400 nm cutoff filter and 510 nm cut-off filter, respectively. In the present study, at first, the NO gas was continuously introduced to the reactor (flow rate: 200 cm^3 min^{-1}) before light irradiation. The initial concentration of NO_x was about 1.0 ppm, and during the experiment, gas containing 1.0 ppm NO_x was passing through the reactor continuously. The photocatalytic reaction was started when the concentration of NO_x at the outlet of the reactor reaching a steady value near 1.0 ppm. The filter was changed so as to evaluate the activity under the irradiation with another wavelength
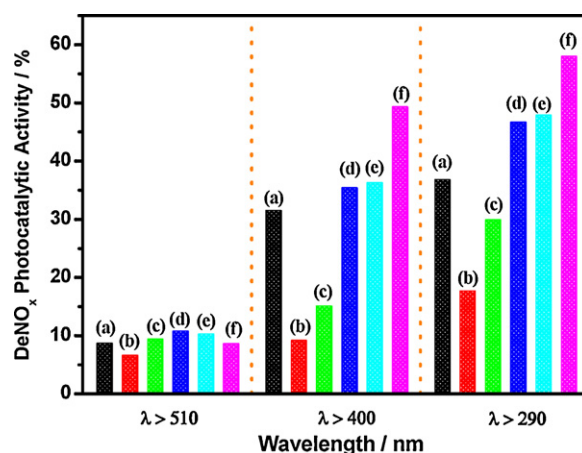

Fig. 8. The Photocatalytic activity in destructing NO_x gas under irradiation with various wavelengths over different photocatalysts: (a) TiO_2 (P25) powder, (b) ZnO nanorod arrays on the glass substrate, (c) ZnO nanotube arrays on the glass substrate, (d) $TiO_{2-x}N_y$ film on the glass substrate, (e) ZnO nanorod arrays/$TiO_{2-x}N_y$ composite on the glass substrate, and (f) ZnO nanotube arrays/$TiO_{2-x}N_y$ composite on the glass substrate.

region. It was obvious that the NO concentration decreased under irradiation of various light wavelengths such as >510 nm, >400 nm and >290 nm, respectively. It was also found that when the light was turned off, the NO concentration returned to its initial level of 1 ppm within 10 min, indicating that light energy is necessary for the oxidation of nitrogen monoxide.

Although the band-gap of the studied materials were all more than 3.2 eV, all samples including TiO_2 (P25) displayed excellent UV light induced photocatalytic activity and relatively weak photocatalytic activity under visible light irradiation. The visible light induced activity of studied materials might be related to the impurity level caused by the residual impurity such as N, C, etc. [39–41]. The same results were presented in our previous research. As expected from the large band gap energy, the photocatalytic activities of both ZnO and commercial TiO_2 under the light of wavelength >510 nm irradiation were quite low. Although the as-prepared pure ZnO nanorod and nanotube showed lower $deNO_x$ photocatalytic activities than those of commercial TiO_2 which has high specific surface area (ca. 55 m^2 g^{-1}), under light of wavelength >400 nm irradiation, actually, the $deNO_x$ ability of ZnO samples were confirmed.

It is well known that photocatalytic activity is strongly related with physical properties such as crystal phase, particle size, specific surface area, crystallinity and morphology [42–44]. It is accepted that the recombination between electrons and holes is difficult to be obtained on a perfect crystal surface, and the number of reaction centers usually increases with increasing specific surface of the catalyst. In our researches, the $TiO_{2-x}N_y$ was prepared by a low-temperature homogeneous precipitation–solvothermal process. So it showed such a high specific surface area as 170 m^2 g^{-1}. At the same time, it was reported that nitrogen doping leads to a narrowing of the band gap by mixing the N 2p and O 2p states and consequently induces visible-light responsive photocatalytic activity [23]. As a result, the nitrogen-doped $TiO_{2-x}N_y$ exhibited higher a NO destruction capability than commercial TiO_2 under irradiation with light of wavelength >290 nm and 400 nm, respectively.

It is very interesting that the photodegradation of NO_x was more efficient by ZnO nanotube arrays than by ZnO nanorod arrays under irradiation with light of wavelength >290 nm and 400 nm, respectively. The NO_x gas could be eliminated almost 30% by ZnO nanotube arrays while ZnO nanorod arrays showed 18% degradation of NO after illuminated by UV light. The enhanced

photocatalytic activity could be ascribed to the unique surface features of its well-aligned structure. Nanotubes differ from nanorods in that they typically had a hollow cavity structure. Obviously, ZnO nanotube arrays had a larger surface area than that of ZnO nanorod arrays with the same length and diameter because nanotubes comprised both an outer and inner surface. The peculiar tubular nanostructure provided more interfaces for adsorption of NO molecules, which greatly increased the photocatalytic activity of ZnO nanotube arrays. At the same time, when the ZnO nanotube arrays were applied as a photocatalysts, the light from the illumination were perfectly trapped in the nanotube arrays and reduplicatively absorbed both inside and outside of the tubes. As nanotubes were hollow, this was most probably due to the contribution of the repetitious diffusion of light among/inside of the hollow tube arrays structure. On the other hand, it is well known that hexagonal wurtzite ZnO rods possess two oppositely charged polar facets $(0\,0\,0\,1)$-Zn and $(0\,0\,0\,-1)$-O which are perpendicular to the $[0\,0\,0\,1]$ direction. As to ZnO nanotubes, the two polar facets were much reduced compared with that of ZnO nanorods, remaining $(1\,0\,-1\,0)$ surfaces. The difference of surface atomic structures should result in a distinct chemical ability and the reported photocatalytic activity for various ZnO planes was different [13,45]. The atomic arrangements on low index planes of the hexagonal prism on ZnO, the $(1\,0\,-1\,0)$ planes are stoichiometric, with equal numbers of exposed Zn^{2+} and O^{2-} ions, and thus they are non-polar with lowest surface energy. While the basal planes, $(0\,0\,0\,1)$ and $(0\,0\,0\,-1)$, are strongly polar, consisting of sheets of Zn^{2+} or O^{2-}. So, the two facets are metastable while the other six side non-polar facets are mostly stable. The instability of two facets is caused by its high surface energy, and the deNO$_x$ reaction reportedly related to oxidation through actively species, such as $^{\bullet}OOH$ and $^{\bullet}O_2^{-}$ [44]. These actively species played an important role in photocatalytic reactions and they were consumed by the above photolysis reactions. For ZnO rods, $(0\,0\,0\,-1)$-O and $(0\,0\,0\,1)$-Zn surface were easier to be attacked by actively species thus showed lower photocatalytic activity than that of nanotubes.

It is obvious that ZnO nanotube arrays/TiO$_{2-x}$N$_y$ composites and ZnO nanorod arrays/TiO$_{2-x}$N$_y$ composites exhibited a much higher photocatalytic activity than that of pure ZnO nanorod arrays, nanotube arrays and pure TiO$_{2-x}$N$_y$, respectively. As observed in Fig. 8, the ZnO nanotube arrays/TiO$_{2-x}$N$_y$ composites exhibited the highest photocatalytic activity among those nanocatalysts under irradiation with light of wavelength >290 nm and 400 nm, respectively. The higher photocatalytic activity of ZnO nanorod or nanotube arrays/TiO$_{2-x}$N$_y$ composites was related to the role of ZnO nanotube or nanorod arrays on the surface of TiO$_{2-x}$N$_y$ film. The fact could be related to the vectorial transfer of electrons and holes, which took place in coupled semiconductors possessing different redox energy levels for their corresponding conduction and valence bands.
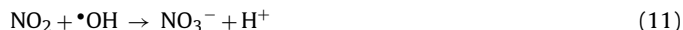
Though the ZnO possesses an energy band similar to that of TiO$_2$, it still plays an important role in electron transport. The charge transport in the ZnO/TiO$_{2-x}$N$_y$ film was no doubt a key step for further increasing the photocatalytic efficiency. The ZnO/TiO$_{2-x}$N$_y$ film excited by photons with energy higher than the gap energy (E_g), a great number of electrons were promoted from valence band (VB) to the conduction band (CB) of ZnO and TiO$_{2-x}$N$_y$, leading to the generation of electron/hole (e^-/h^+) pairs. The electrons transferred from the CB of ZnO to the CB of TiO$_{2-x}$N$_y$, and conversely, the holes transferred from the VB of TiO$_{2-x}$N$_y$ to the VB of ZnO give rise to decrease the pairs' recombination rate. Obviously, the energy level for electron injection was decreased after TiO$_2$ film-cover the surface of ZnO film, which increased the driving force for electron injection and hence reduced recombination between electrons and holes. On the other hand, ZnO could increase concentration of free electrons in the CB of TiO$_2$; this result implied that the charge recombination was reduced in the process of electron transport. All above of results increased the availability of the pairs on the surface of the photocatalyst and consequently an improvement of the occurrence of redox processes could be expected. This efficient charge separation increased the lifetime of the charge carriers and enhanced the efficiency of the interfacial charge transferring to adsorbed substrates. The vectorial charge transferred from one semiconductor to another with suitable band edge positions that was thermodynamically favorable could increase the lifetime of the charge carriers thus promoting the interfacial charge transfer and catalytic efficiency.

At the present time, the mechanism of NO photoxidation by oxygen on photocatalysts is not known in detail. Reaction Eqs. (6)–(12) represent the possible surface processes occurring during the photocatalytic decomposition of NO on ZnO surfaces. It is accepted that photocatalyst particles absorb light of energy greater than the band gap to generate electron/hole pairs (Eq. (6)). The electrons are photoinduced to the conduction band ($e_{CB}^{\bullet-}$) and the holes in the valence band ($h_{VB}^{\bullet+}$). It is often suggested the key role of $^{\bullet}OH$ radicals and anion-radicals $^{\bullet}O_2^{-}$ formed upon the capture of photogenerated holes and electrons by surface hydroxyls and oxygen molecules. In the presence of oxygen, these photoinduced electrons are immediately trapped by the molecular oxygen to form $^{\bullet}O^{2-}$ (Eq. (8)), which can then generate active $^{\bullet}OOH$ radicals (Eq. (9)). At the same time, the holes are trapped by water in the air to produce hydroxyl radicals (Eq. (10)). The deNO$_x$ reaction reportedly relates to oxidation through active oxygen species, such as $^{\bullet}OH$ and $^{\bullet}O_2^{-}$.

Nitrogen monoxide reacted with these reactive radicals, molecular oxygen, and a very small amount of water in the air (humidity was about 25% in the present study) to produce HNO$_2$ or HNO$_3$ (Eqs. (10) and (11)). It has also been reported that about 20% of the nitrogen monoxide decomposed directly into nitrogen and oxygen [46]. The photocatalytic oxidation of NO produces two major products: NO$_2$ gas and HNO$_3$ on catalyst surface. HNO$_2$ is a minor species on catalyst surface. In the NO$_x$ atmosphere, the NO$_x$ molecule may have trapped the superoxide radical $^{\bullet}O^{2-}$ to form NO$_3^{-}$ (Eq. (12)). Finally, the nitric acid forms at the catalyst surface. The activity of photocatalyst diminishes with the accumulation of acid.

The possible photoreactions on the photocatalysts are proposed as

$$ZnO \xrightarrow{h\nu} ZnO \times (h_{VB}^{+} + e_{CB}^{-}) \tag{6}$$

$$h_{VB}^{\bullet+} + H_2O \rightarrow {^{\bullet}OH} + H^{+} \tag{7}$$

$$e_{CB}^{\bullet-} + O_2 \rightarrow {^{\bullet}O_2^{-}} \tag{8}$$

$${^{\bullet}O_2^{-}} + H^{+} \rightarrow {^{\bullet}OOH} \tag{9}$$

$$NO + 2OH \rightarrow NO_2 + H_2O \tag{10}$$

$$NO_2 + {^{\bullet}OH} \rightarrow NO_3^{-} + H^{+} \tag{11}$$

$$NO_x + {^{\bullet}O_2^{-}} \rightarrow NO_3^{-} \tag{12}$$

4. Conclusions

In summary, ZnO crystals with developed superstructures, such as nanorod arrays and nanotube arrays were successfully synthesized by a mild solvothermal process via a surfactant-assisted chemical etching strategy. At the same time, the ZnO/TiO$_{2-x}$N$_y$ heterojunction composites were also successfully prepared. The investigation of photocatalytic ability indicated that the ZnO nanotube arrays/TiO$_{2-x}$N$_y$ composites have excellent photocatalytic activities for the decomposition of NO when compared with the performance of pure ZnO nanorods, nanotube, TiO$_2$ (P25) and TiO$_{2-x}$N$_y$. This is because (i) the ZnO nanotube arrays/TiO$_{2-x}$N$_y$ composites have unique surface features of its

well-aligned structure, and (ii) the heterojunction structure can promote an increase in the charge separation of the photogenerated electrons and holes within the composite nanostructures to enhance photocatalytic reaction. This novel photocatalyst can achieve high quantum efficiency and lead to high photocatalytic activity.

Furthermore, the ZnO nanorods, nanotube arrays/$TiO_{2-x}N_y$ composites film could be easily regenerated by rain water due to their one-dimensional nanostructure property, if the photocatalyst was applied as thin film format on the surface of building materials, natural solar energy could be used for atmospheric purification. So, it is expected that the ZnO nanorods, nanotube arrays/$TiO_{2-x}N_y$ composites with high photocatalytic activity will greatly promote their industrial application for environmental applications.

Acknowledgments

References

[1] Y.L. Lai, M. Meng, Y.F. Yu, X.T. Wang, T. Ding, Applied Catalysis B 105 (2011) 335–345.
[2] Q.F. Zhang, C.S. Dandeneau, X.Y. Zhou, G.Z. Cao, Advanced Materials 21 (2009) 4087–4108.
[3] Z.L. Wang, Materials Today 7 (2004) 26–33.
[4] X.Y. Kong, Y. Ding, R.S. Yang, Z.L. Wang, Science 303 (2004) 1348–1351.
[5] C.S. Lao, P.X. Gao, R.S. Yang, Y. Zhang, Y. Dai, Z.L. Wang, Chemical Physics Letters 417 (2005) 359–363.
[6] P.X. Gao, Z.L. Wang, Small 1 (2005) 945–949.
[7] P.X. Gao, Z.L. Wang, Applied Physics Letters 84 (2004) 2283–2285.
[8] Q.H. Zhang, W.G. Fan, L. Gao, Applied Catalysis B 76 (2007) 168–173.
[9] Y. Daia, Y. Zhang, Z.L. Wang, Solid State Communications 126 (2003) 629–633.
[10] C.C. Chen, Journal of Molecular Catalysis A: Chemical 264 (2007) 82–92.
[11] J. Nishio, M. Tokumura, H.T. Znad, Y. Kawase, Journal of Hazardous Materials 138 (2006) 106–115.
[12] H. Wang, C. Xie, W. Zhang, S. Cai, Z. Yang, Y. Gui, Journal of Hazardous Materials 141 (2006) 645–652.
[13] D.W. Chu, Y. Masuda, T. Ohji, K. Kato, Langmuir 26 (2010) 2811–2815.
[14] Y.J. Xing, Z.H. Xi, Z.Q. Xue, X.D. Zhang, J.H. Song, R.M. Wang, J. Xu, Y. Song, S.L. Zhang, D.P. Yu, Applied Physics Letters 83 (2003) 1689–1691.
[15] J.Q. Hu, Y. Bando, Applied Physics Letters 82 (2003) 1401–1403.
[16] G.S. Wu, T. Xie, X.Y. Yuan, Y. Li, L. Yang, Y.H. Xiao, L.D. Zhang, Solid State Communications 134 (2005) 485–489.
[17] S. Yin, T. Sato, Journal of Materials Chemistry 15 (2005) 4584–4587.
[18] H.D. Yu, Z.P. Zhang, M.Y. Han, X.T. Hao, F.R. Zhu, Journal of the American Chemical Society 127 (2005) 2378–2379.
[19] L. Layssieres, K. Keis, A. Hagfeldt, S.E. Lindquist, Chemistry of Materials 13 (2001) 4395–4398.
[20] L. Vayssieres, N. Beermann, S.E. Lindquist, A. Hagfeldt, Chemistry of Materials 13 (2001) 233–235.
[21] L. Vayssieres, A. Manthiram, Journal of Physical Chemistry B 107 (2003) 2623–2625.
[22] L. Vayssieres, M. Graetzel, Angewandte Chemie International Edition 116 (2004) 3752–3756.
[23] R. Asahi, T. Morikawa, T. Ohwaki, K. Aoki, Y. Taga, Science 293 (2001) 269–271.
[24] S. Yin, Y. Aita, M. Komatsu, J. Wang, Q. Tang, T. Sato, Journal of Materials Chemistry 15 (2005) 674–682.
[25] Japanese Standards Association Japanese Industrial Standard (JIS R 1701-1:2004(J)), Test method for air purification performance of photocatalytic materials – Part 1: removal of nitric oxide, Established on 2004-01-20.
[26] G. Cao, L.K. Rabenberg, C.M. Nunn, T.E. Mallouk, Chemistry of Materials 3 (1997) 149–156.
[27] S.T. Tan, B.J. Chen, X.W. Sun, W.J. Fan, H.S. Kwok, X.H. Zhang, S.J. Chua, Journal of Applied Physics 98 (2005) 013501–14156.
[28] X. Zhao, W.Q. Yao, Y. Wu, S.C. Zhang, H.P. Yang, Y.F. Zhu, Journal of Solid State Chemistry 179 (2006) 2562–2570.
[29] M.H. Huang, Y.Y. Wu, H. Feick, N. Tran, E. Weber, P.D. Yang, Advanced Materials 13 (2001) 113–116.
[30] T. Ivanova, A. Harizanova, M. Surtchev, Materials Letters 55 (2002), 327–323.
[31] H.M. Zhang, X. Quan, S. Chen, H.M. Zhao, Applied Physics A 89 (2007) 673–679.
[32] G.K. Mor, O.K. Varghese, M. Paulose, C.A. Grimes, Advanced Functional Materials 15 (2005) 1291–1296.
[33] P. Chen, I.W. Chen, Journal of the American Ceramic Society 76 (1993) 1577–1583.
[34] J.M. Dreyfors, S.B. Jones, Y. Sayed, American Industrial Hygiene Association Journal 50 (1989) 579–585.
[35] H.Q. Wang, G.H. Li, L.C. Jia, G.Z. Wang, C.J. Tang, Journal of Physical Chemistry C 112 (2008) 11738–11743.
[36] H.Q. Wang, M. Li, L.C. Jia, G.Z. Wang, Y.X. Zhang, G.H. Li, Nanoscale Research Letters 5 (2010) 1102–1106.
[37] R.A. Laudise, A.A. Ballman, Journal of Physical Chemistry B 64 (1960) 688–691.
[38] E.S. Jang, J.H. Won, S.J. Hwang, J.H. Choy, Advanced Materials 18 (2006) 3309–3312.
[39] R.I. Bickley, T. Gonzalez-Carreno, J.S. Lees, L. Palmisano, R.J.D. Tilley, Journal of Solid State Chemistry 92 (1991) 178–190.
[40] J. Kirchnerova, M.-L.H. Cohen, C. Guy, D. Klvana, Applied Catalysis A 282 (2005) 321–332.
[41] T. Egerton, J. Mattinson, Journal of Photochemistry and Photobiology A 194 (2008) 283–289.
[42] J.S. Dalton, P.A. Janes, N.G. Jones, J.A. Nicholson, K.R. Halam, G.C. Allen, Environmental Pollution 120 (2002) 415–422.
[43] P.L. Zhang, X.W. Liu, S. Yin, T. Sato, Applied Catalysis B 93 (2010) 299–303.
[44] S. Yin, B. Liu, P.L. Zhang, T. Morikawa, K.I. Yamanaka, T. Sato, Journal of Physical Chemistry C 112 (2008) 12425–12431.
[45] J. Bae, J.B. Han, X.M. Zhang, M. Wei, X. Duan, Y. Zhang, Z.L. Wang, Journal of Physical Chemistry C 113 (2009) 10379–10383.
[46] M. Anpo (Ed.), Recent Development on Visible Light Response Type Photocatalyst, NTS, Tokyo, 2002, p. p. 9, ISBN 4-86043-009-03.